Appl. Phys. B 88, 317–325 (2007)
DOI: 10.1007/s00340-007-2691-x

Applied Physics B
Lasers and Optics

D. LISAK[1,2]
J.T. HODGES[1,✉]

High-resolution cavity ring-down spectroscopy measurements of blended H_2O transitions

[1] Process Measurements Division, National Institute of Standards and Technology, 100 Bureau Drive, Gaithersburg, MD 20899, USA
[2] Instytut Fizyki, Uniwersytet Mikołaja Kopernika, ul. Grudziadzka 5/7, 87-100 Toruń, Poland

Received: 22 February 2007/Revised version: 7 May 2007
Published online: 19 June 2007 •

ABSTRACT We probed four closely spaced rovibrational water vapor absorption transitions near $\tilde{\nu} = 7100\,\mathrm{cm}^{-1}$ using frequency-stabilized cavity ring-down spectroscopy. Room-temperature spectra were acquired for pure water vapor in the Doppler limit and for mixtures containing $\approx 6.6\,\mu\mathrm{mol\,mol}^{-1}$ of water vapor in N_2 at total gas pressures ranging from 6.5 kPa to 53 kPa. By measuring Lamb dips for each transition, we demonstrated a resolution of 50 kHz and determined relative transition frequencies with an uncertainty < 0.4 MHz over a 10 GHz range. Pressure-induced broadening, collisional narrowing coefficients of the component transitions and line areas were retrieved by fits of model line shapes to the measured spectra. Standard and advanced models were considered including those which incorporated the combined effects of collisional narrowing and speed-dependent line broadening and line shifting. By measuring water vapor concentration with a transfer standard hygrometer, we determined line intensities in terms of measured line areas with a combined relative uncertainty of 0.6%.

PACS 33.20.-t; 33.70.Jg; 33.70.Fd; 42.62.Fi

1 Introduction

From a theoretical perspective, molecular line intensities can be highly sensitive to detailed physical aspects that underpin absorption transitions between quantum states [1]. However, high-accuracy measurements of molecular line intensities are often difficult to achieve, thus impeding experimental validation of higher-order theoretical predictions for line intensities. As intrinsic properties which correspond to specific transition moments of a molecule, line intensities are required in many measurement applications including the spectroscopic determination of concentration, temperature and isotope ratios in atmospheric samples. Line intensities are typically determined in the laboratory by preparing an absorbing sample of known concentration, measuring the absorption spectrum at high resolution and fitting appropriate line shape models to the observed spectra. Uncertainties arising from instrumentation-related effects (non-linearities, spectral resolution and distortions, interferences, noise etc.) coupled with limitations of line shape models limit the accuracy of line intensity determinations. Measurements of line intensity are especially difficult for species where absorption transitions are nearly coincident and where there is substantial blending of Doppler- and pressure-broadened lines. Indeed, to date there exist relatively few observed line intensities having combined relative uncertainties at the 0.5%-level or below such as those reported for near-infrared spectra of CO_2 [2, 3] and CO [4].

We have shown that frequency-stabilized cavity ring-down spectroscopy (FS-CRDS) can be used for low-uncertainty line shape measurements of water vapor spectra [5]. In this previous work we fit line shape models incorporating effects of collisional narrowing, and/or speed-dependent broadening effects to high-resolution FS-CRDS spectra of isolated transitions. We demonstrated that the best line shape models included the effects of collisional narrowing and speed-dependent broadening yielding line intensities that were indistinguishable at the 0.2% level. Other models lacking these two effects gave systematic relative uncertainties in line intensity > 1%. For line center determination and illustration of frequency resolution, we also demonstrated that FS-CRDS can be used to measure MHz-wide Doppler-free saturation dips with a resolution better than 50 kHz.

The primary aim of this study is to quantify the uncertainty with which FS-CRDS can be used to measure line intensities for closely spaced and overlapping absorption transitions. Particular attention is paid to the resolution and uncertainty in the observed spectrum frequency axis. In conjunction with FS-CRDS which provides accurate determination of line shapes, we consider absorption spectra of water vapor and we employ techniques for water vapor sample preparation that are directly traceable to primary methods of humidity generation. Given the importance of water vapor spectroscopy and the challenges associated with preparing samples of known water vapor concentration, we intend these results to be a useful benchmark against which other low-uncertainty measurements of line intensity may be compared.

The 1.39 μm region was recently investigated by many authors. Because there are many relatively strong H_2O lines in this region which are accessible with tunable diode lasers, these transitions were used in practical applications e.g. the development of a spectroscopic hygrometer [6] a temperature sensor for combustion gases [7] and isotope ratio measurements for ^{16}O-,^{17}O- and ^{18}O-containing isotopologues of

✉ Fax: +1 301 869 5924, E-mail: joseph.hodges@nist.gov

H_2O [8]. Many transitions from this spectral region other than those reported here were investigated with high resolution laser spectroscopy, see [9–12] and references therein.

In this article we present a series of high resolution spectra near wave number $\tilde{\nu} = \lambda^{-1} = 7156.8\,\mathrm{cm}^{-1}$ taken under conditions of varying pressure with N_2 as the collisional partner. We report the magnitudes and standard uncertainties in the line intensities, relative transition frequencies and foreign-broadening and shifting coefficients. The set of four water vapor transitions considered labeled *A*, *B*, *C*, and *D*, respectively and their assignments and frequencies from HITRAN 2004 [13] are given in Table 1.

2 Measurement technique

2.1 *Blended spectra and Beer's law*

The Beer–Lambert law states that the fractional reduction in light intensity per-unit-length of propagation through a homogeneous absorbing medium is given by the absorption coefficient $\alpha(\nu)$. For an absorbing gas sample $\alpha(\nu)$ can be represented as a superposition of individual transitions i given by $\sum_i \alpha_i(\nu) = n_a c \sum_i S_i g_i(\nu - \nu_i)$, where ν is the radiation frequency, n_a is the absorber concentration, ν_i is the transition frequency, S_i is the line intensity and c is the speed of light. The term g_i is the line shape function which in general depends on the total composition of the gas mixture. Note that the line shape function is normalized so that $\int g_i \,\mathrm{d}\nu = 1$. It follows that the line area, defined as $A_i = \int \mathrm{d}\nu \alpha_i(\nu) = n_a c S_i$, relates the area under an observed spectral peak to a specific line intensity. In general g_i depends upon the absorber and carrier gas concentration, and embodies all mechanisms affecting the line shape and line position. In this model we have assumed a single absorbing species and we have neglected effects of saturation and line mixing. Note that since the quantity $n_a S_i$ appears as a product, the measurement of $\alpha(\nu)$ is insufficient to determine the S_i without independent determination of n_a, thus linking uncertainty in S_i to uncertainty in n_a.

2.2 *Frequency-stabilized cavity ring-down spectroscopy*

As described previously, FS-CRDS uses the stabilized and tunable comb of resonant frequencies of the ring-down cavity to provide a linear and accurate frequency axis [14, 15]. This method distinguishes FS-CRDS from most other implementations of CRDS where an external étalon or reference spectrum is used to calibrate the frequency detuning of the probe laser. The recently demonstrated optical-feedback CRDS technique [16, 17] yields a spectrum frequency axis similar to that of FS-CRDS, but which lacks two important aspects of FS-CRDS: active stabilization and fine shifting of the ring-down cavity frequency comb, with the latter enabling sampling of the spectrum at intervals less than the cavity free-spectral range (FSR). A comparison of FS-CRDS to other commonly used CRDS schemes was presented in [6] where it was demonstrated that thermal-induced drift of cavity resonances of an unstabilized ring-down cavity can distort the measured line shape.

Excitation with a narrowband continuous wave (cw) probe laser enables the selective excitation of longitudinal modes of the stabilized cavity's TEM_{00}, thus ensuring single-exponential decays and eliminating unpredictable effects associated with multi-mode excitation and cavity drift. Cavity intensity decay rates are measured by fitting the time dependence of the exiting cavity intensity to an exponential decay. In CRDS, the component of the intensity decay rate caused by sample absorption is $k_a(\nu) = c\alpha(\nu)$. The total intensity decay rate is the sum $k(\nu) = k_b(\nu) + k_a(\nu)$ where $k_b(\nu)$ represents all other contributions to the cavity's intensity decay rate (possibly including the wings of distant absorption features not explicitly modeled in the line shape analysis). Typically, $k_b(\nu)$ acts as a well-behaved baseline feature with a weak dependence on ν and is treated as one or more fit parameters in modeling the observed spectra. Note that because absorption is manifest as an increase in the intensity decay rate, neither the cavity length nor the incident beam intensity is required to determine $\alpha(\nu)$. This unique property distinguishes CRDS from other forms of absorption spectroscopy in which absorbance is determined by the fractional change in intensity that is transmitted through a specified pathlength.

transition	$\tilde{\nu}(\mathrm{cm}^{-1})$	(J', K'_a, K'_c)	(J'', K''_a, K''_c)
A	7156.723	4, 4, 1	5, 3, 2
B	7156.817	3, 1, 2	3, 2, 1
C	7157.044	2, 1, 1	2, 2, 0
D	7157.173	3, 3, 1	4, 2, 2

TABLE 1 Summary of $H_2^{16}O$ transitions from $2\nu_1$ vibrational band observed here. Assignments and line positions $\tilde{\nu}$ are taken from [13] and correspond to 0 pressure shift. (J', K'_a, K'_c) and (J'', K''_a, K''_c) are rotational quanta of the upper and lower states, respectively

3 Experimental apparatus

3.1 *General description*

The FS-CRDS setup was nearly identical to that described in [14, 15], the most important exceptions being a different probe laser and the addition of an I_2-stabilized He-Ne laser to monitor slow frequency drifts in the cavity locking frequency-stabilized He-Ne laser. The probe laser was a cw external cavity diode laser (ECDL) with a short-term linewidth of ≈ 1 MHz, and incident power of ≈ 5 mW. Sample gas pressure p was monitored using a pair of calibrated capacitance diaphragm gauges, corresponding to 13.3 kPa and 133 kPa full-scale responses, respectively. The gas temperature T was inferred from a 100 Ω platinum resistance thermometer mounted in good thermal contact with an exterior surface of the ring-down cell. Since all measurements were made at room temperature, gradients between the gas and wall temperatures were negligible.

3.2 *Sample preparation*

Water vapor samples in N_2 carrier gas were produced by a permeation tube moisture generator (PTMG). This system generated a water vapor molar fraction $x_w \approx 6.6 \times 10^6\,\mu\mathrm{mol\,mol}^{-1}$ in the sample stream, at a total flow rate $Q \approx 0.75$ std. L min^{-1}. For the line intensity determinations, approximately one half of the PTMG output stream was diverted to a standards-grade chilled mirror hygrometer (CMH) placed in parallel with the ring-down

cavity and used to measure x_w via the frost-point temperature. The remainder of the flow stream passed through the ring-down cavity. The CMH was calibrated directly against a primary thermodynamic humidity generator maintained at NIST [18]. Ancillary data acquired included T and p measured at the ring-down cavity, and the frost-point temperature T_f and pressure p_f of the sample gas in the CMH. The CMH-measured water vapor molar fraction was given by $x_w = f(T_f, p_f)e_w(T_f)/p_f$ where where f is the enhancement factor for mixtures of water vapor and N_2 [19] and e_w is the saturation vapor pressure of ice [20]. Assuming an ideal gas mixture in the ring-down cell, the water vapor concentration was given by $n_a = x_w p(k_B T)^{-1}$ where k_B represents the Boltzmann constant.

The combined standard relative uncertainty for the water vapor concentration in the cell, $u_{c,r}(n_a)$ was estimated to be 0.54% assuming $u^2_{c,r}(n_a)$ is given by $u_r(x_w)^2 + u_r(p)^2 + u_r(T)^2 + u_r(k_B)^2$. This expansion includes type B uncertainties in the measurement of x_w originating from 1) the CMH measurement of (0.49%), 2) the primary thermodynamic standard humidity generator used to calibrate the CMH (0.20%), and 3) the water vapor background concentration in ring-down cell (0.1%). The systematic uncertainties from measurements of p, T and k_B contributed less than 0.1% relative uncertainty to the measurement of n_a.

3.3 *Spectrum detuning axis*

In the FS-CRDS method implemented here, the spectrum detuning axis is linked to the ring-down cavity's stabilized comb of resonant frequencies of the fundamental transverse mode TEM_{00}. We emphasize that the comb of resonant frequencies represents a natural and precise scale for the abscissae of cavity ring-down spectra. First, the radiation absorbed by the sample must be within the bandwidth of these resonances irrespective of frequency fluctuations in the probe laser spectrum. Second, these resonances are typically much narrower (< 5 kHz for this experiment) than the probe laser line width (time-averaged value > 1 MHz). Thus the FS-CRDS approach yields an exceptionally linear and high-resolution detuning axis, surpassing the performance of detuning axes acquired by interpolating between transmission peaks of the probe laser through external ètalons or by frequency calibration against reference spectra. In the present work the ring-down cavity is actively length-stabilized with respect to a frequency-stabilized He-Ne locking laser emitting at wavelength ≈ 633 nm, and spectra are acquired by locking the probe laser frequency to sequential longitudinal modes of the stabilized ring-down cavity. The cavity locking servo has a bandwidth of ≈ 10 Hz and eliminates thermal drift in the cavity length and forces the cavity to maintain resonance with the He-Ne locking laser. The long-term frequency stability of the locking laser is ≈ 1 MHz. Finer frequency steps are realized by shifting the locking laser frequency and hence the comb of TEM_{00} cavity resonances using a double-passed acousto-optic modulator (AOM) as discussed in [14]. Slow drifts in the cavity length caused by frequency drifts in the locking He-Ne laser frequency are measured by tracking the beat note f_b produced by interference with an I_2-stabilized He-Ne laser (frequency stability of 5 kHz/°C). As previously shown [21, 22] an optical comb was mapped onto a high-finesse cavity over a 1 nm spectral range using standard high-reflectivity mirrors. More recently, an optical frequency comb was mapped onto a ring-down cavity over a spectral range exceeding 15 nm using low group-delay dispersion mirrors [23, 24]. These results are consistent with previous predictions [25], and indicate that dispersion in ring-down cavities can be neglected for sufficiently small bandwidths and for sufficiently weakly absorbing samples. Treating the cavity comb spacing as a constant independent of frequency gives for the detuning relative to the first point in the spectrum,

$$\Delta\nu = \frac{c}{2n\ell}\Delta q - (2\Delta f_A - \Delta f_b)\frac{\nu}{\nu_l} + \delta\nu_q\,, \tag{1}$$

where ν and ν_l are the respective probe laser and cavity-locking laser frequencies within the bandwidths of local resonant frequencies of the ring-down cavity, ℓ is the empty cavity length, n is the real part of the refractive index of the medium evaluated at ν, q is the longitudinal mode order of the ring-down cavity mode, $\Delta f_A = f_A - f_{A,0}$ is the change in AOM frequency where f_A is the AOM frequency, and $f_{A,0}$ is the AOM frequency at $\Delta\nu = \Delta q = 0$. The term Δf_b represents the change in ν_l as measured by the beat note measurement. Given the relatively small frequency shifts considered here, the quantity ν/ν_l can be treated as a constant, so that frequency shifts of the ring-down cavity at the probe laser wavelength are linearly dependent on Δq and Δf_A. We note that the optical path length and the FSR, which is given by $c(2n\ell)^{-1}$, depend on the average gas density. Neglecting dispersion effects associated with the weakly absorbing sample gas, we use the relation $n - 1 = C(\nu)n_g k_B T$, where C is the gas refractivity per unit pressure and n_g is the gas concentration, to account for the density dependence of the FSR.

In practice, the last term $\delta\nu_q = \nu - \nu_q$ of (1) is neglected as its average value is expected to be zero and it corresponds to small random detunings of the probe laser with respect to the local cavity resonance frequency. This term is associated with uncompensated fluctuations in the cavity length and gas density. It also accounts for frequency fluctuations in the probe laser that are within the instantaneous cavity line width. $\delta\nu_q$ introduces a minimum uncertainty in $u(\Delta\nu)$ given by $\sigma(\delta\nu_q)$, where $\sigma(\delta\nu_q)$ is the standard deviation of the distribution of $\delta\nu_q$ values. In the absence of path length fluctuations $u(\delta\nu_q)$ is nominally equal to the half width at half maximum (HWHM) of the ring-down cavity resonance: a quantity representing the minimum frequency resolution to be expected with the FS-CRDS technique assuming excitation bandwidths exceeding the cavity line width.

Using (1), we derive the square of the combined standard uncertainty of $\Delta\nu$ to be

$$u_c^2(\Delta\nu) = \Delta q^2 u^2(\mathrm{FSR}) + \left(4u^2(f_A) + u^2(f_b)\right)\frac{\nu^2}{\nu_l^2} + u^2(\delta\nu_q)\,. \tag{2}$$

Evaluation of the preceding equation requires estimation of the standard uncertainties $u(\mathrm{FSR})$, $u(f_A)$, $u(f_b)$, and $u(\delta\nu_q)$.

3.3.1 Free-spectral range measurement. We determined the empty cavity free-spectral-range ($\mathrm{FSR}_0 = c(2\ell)^{-1}$) by locking the probe laser to successive longitudinal modes of the

cavity and measuring the probe laser frequency with a scanning Michelson-interferometer wavelength meter having a combined standard uncertainty of 60 MHz and resolution of 20 MHz. Measurements were made at vacuum conditions where $n-1<10^{-9}$. With no ambiguity in the mode order shift Δq, the FSR was determined simply by the slope of the measured frequency versus Δq. Measurements spanning $\Delta q=1400$ yielded $\mathrm{FSR}_0=203.211(6)$ MHz. The FSR was independently determined by measuring the frequency separation between several water vapor transitions tabulated in HITRAN 2004. These measurements of the FSR agreed with the wavelength-meter-based determination, although they were more uncertain by a factor of 5 because of the uncertainty in the water vapor transition frequencies. Note that for detuning through a frequency range $\Delta\nu=\Delta q\mathrm{FSR}$, the systematic uncertainty in detuning is given by $u(\Delta\nu)=\Delta q u(\mathrm{FSR})$, where for the present system $u(\mathrm{FSR})=6$ kHz.

For variations in gas pressure exceeding ≈ 4 kPa the cavity length-stabilization servo must be interrupted because of the finite displacement range of the pzt-actuated mirror. Changes in the cavity length induced by thermal drift of the assembly occurring during the unlocked cavity condition can alter the empty-cavity FSR that is realized after relocking the cavity length. Correlation of the ring-down cavity mirror-actuating pzt-voltage with system temperature indicated a change in cavity FSR per-unit temperature $\approx -1.2\,\mathrm{kHz/°C}$. With a maximum measured temperature excursion of 0.6 °C, this effect yields the component uncertainty $u(\mathrm{FSR})\approx 0.7$ kHz, which is far less than the uncertainty in FSR-determination given above. In contrast, systematic changes in the FSR associated with the change in gas density were taken into account as discussed above. For this correction we used $C\approx 2.9\times10^{-6}\,\mathrm{kPa}^{-1}$, taken from air refractive index correlations [26] and modified to the case of pure N_2 using the approximate relation $(n-1)_{0_2}/(n-1)_{N_2}\approx 0.9$. This correction givs $\Delta\mathrm{FSR}\approx -32$ kHz at $p=55$ kPa.

When the ring-down cavity is locked to the He-Ne reference laser and held at a given nominal pressure, slow variations in the gas pressure Δp will induce a shift in the ν_q given by $\delta\nu_q=\Delta p\,\mathrm{d}\nu_q/\mathrm{d}p$. This effect, discussed in detail in [27] is a consequence of dispersion in the refractive index of the medium. Using a measured value $\Delta p=2.5$ Pa, and $\mathrm{d}\nu_q/\mathrm{d}p\approx 6.4\,\mathrm{MHz\,kPa}^{-1}$ [27], we estimate $\delta\nu_q=16.3$ kHz. Another pressure effect on ν_q is associated with resonant acoustic fields within the ring-down cell are driven by external perturbations (table and pump vibrations, gas flow, etc.) and can be manifest as standing waves within the ring-down cavity. Fluctuations of this sort that are not compensated by the cavity locking servo have spatial and temporal distributions which lead to an effective broadening of ν_q about its mean value. We measured the acoustic noise in the ring-down cell with a microphone located at the position of the fixed cavity mirror. Noise spectra of the microphone were recorded with a spectrum analyzer at atmospheric pressure and at flow conditions of the measurements reported here. The broadening of $\delta\nu_q$ due to this acoustic effect was estimated to be $N_\mathrm{a}^{-1/2}q\mathrm{FSR}C(\nu_q)\left[\int w(f_\mathrm{a})\eta_p(f_\mathrm{a})\,\mathrm{d}f_\mathrm{a}\right]^{1/2}$, where $N_\mathrm{a}^{-1/2}$ is the number of ring-down acquisitions at a given frequency detuning, $\eta_\mathrm{p}(f_\mathrm{a})$ is the measured power spectral density of pressure fluctuations, $w(f_\mathrm{a})\approx q_\mathrm{ac}^{-2}$ is a weighting factor accounting for the spatial average of gas density over the cavity path length in which q_ac is the mode order of the acoustic field, and f_a is the acoustic frequency. The lower limit of integration range is ≈ 10 Hz which corresponds to the high-frequency cutoff of the cavity-locking servo. Setting $N_\mathrm{a}=200$, we estimate the acoustic broadening of $\delta\nu_q$ to be ≈ 6 kHz.

When there is a net flow rate of gas through the ring-down cell, there will be a non-zero mean gas velocity in the laboratory frame. This velocity difference will systematically Doppler shift the resonant frequencies of the counter-propagating beams that comprise the recirculating radiation field in the ring-down mode. These resonant frequencies will be shifted by equal and opposite amounts. This splitting of the resonances will diminish with increasing pressure at fixed total flow rate. We estimate a maximum split of 1.4 MHz at the minimum pressure condition considered here given by $p=6.67$ kPa condition. For the case of a static charge (corresponding to the Doppler-broadened spectra shown below), Doppler splitting of ν_q due to bulk gas velocity will obviously not occur.

To illustrate the stability of the locking laser and the precision of the beat-note correction Fig. 1 shows $f_\mathrm{b}(t)$. Although exhibiting slow fluctuations, the uncertainty in the average beat frequency $u(f_\mathrm{b})$ was found to be ≈ 50 kHz, causing an uncertainty $u(\nu_q)<u(f_\mathrm{b})\nu/\nu_\mathrm{l}=23$ kHz. The combined

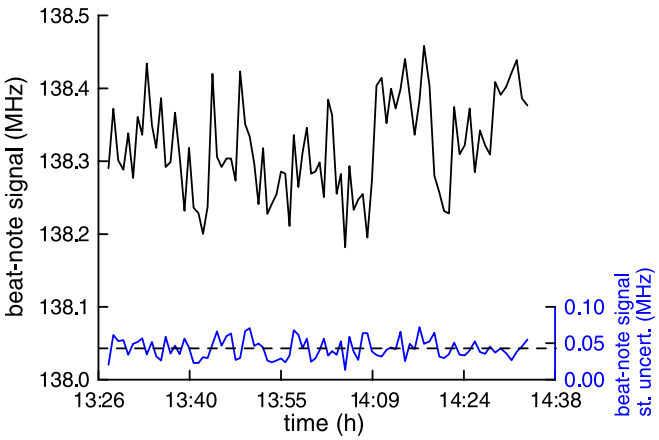

FIGURE 1 *Upper panel*. Time dependence of beat-note frequency Δf_b produced by interference of locking He-Ne laser and I_2-stabilized He-Ne laser. *Lower panel*. Corresponding standard deviation $\sigma(f_\mathrm{b})$ based on 3 s averaging time. *Dashed line* gives the mean value $\langle\sigma(f_\mathrm{b})\rangle\simeq 50$ kHz

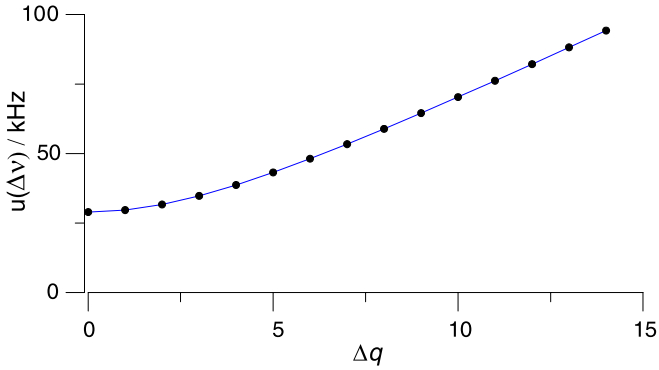

FIGURE 2 Combined standard uncertainty for FS-CRDS detuning axis from (2) based on parameters given in Table 2

x_i	$u(\nu_q(x_i))$	driving quantity	type
f_b	23.0 kHz	uncertainty in beat note	A
$\delta\nu_q$	16.3 kHz	broadening by pressure drift	A
$\delta\nu_q$	6.0 kHz	broadening by acoustic fluctuations	A
ν_r	4.7 kHz	stability of I_2-stabilized He-Ne reference laser, $u(T) = 1\,^\circ$C	A
ν_q	3.2 kHz	halfwidth of cavity resonance, $L_{tot} = 10^{-4}$	B
f_a	1.5 kHz	uncertainty in AOM frequency	A
FSR	6.0 kHz	uncertainty in 0-pressure determination of cavity FSR	B
FSR	1.6 kHz	uncertainty in $n-1$ determination, $p = 53.3$ kPa	B
FSR	1.2 kHz	uncertainty in cavity length change, $u(T) = 1\,^\circ$C	A
FSR	1.1 kHz	absorption-induced dispersion, $L_{abs} = 5\times10^{-5}$	B
$u(\text{FSR}) = \left[\sum u_i^2(\text{FSR})\right]^{1/2}$	6.4 kHz	combined uncertainty in FSR	

TABLE 2 Uncertainty components for FS-CRDS detuning axis for the static charge condition. FSR($p = 0$) = 203.211(6) MHz

type A uncertainty in ν_q is ≈ 29 kHz, consistent with our ability to resolve Lamb dips in the ring-down spectra with full-widths < 0.5 MHz and with a repeatibility better than 50 kHz [5]. A summary of the uncertainty analysis for the detuning axis in the static charge limit is given in Table 2. Finally, Fig. 2 shows $u_c(\Delta\nu)$ as function of Δq for the parameters given in Table 2. For $\Delta q > 6$, $u_c(\Delta\nu)$ is dominated by u(FSR) and asymptotically approaches ΔqFSR.

4 Results

4.1 *Low pressure spectra and Lamb-dips*

At sufficiently low pressures where the line shapes are dominated by Doppler broadening the four transitions under investigation do not exhibit significant blending. We investigated this limiting case by probing the background water vapor that had desorbed from the walls of the evacuated ring-down cavity. The water vapor concentration was adjusted to the desired level by slowly pumping on the ring-down cavity and monitoring the peak absorption losses. The absorption spectrum and Gaussian fits for this low-pressure case ($p = 38.3$ mPa) are shown in Fig. 3. The relative positions of the transitions were inferred from the set of four fitted Guassian line shapes. As previously reported [5], we were also able to measure narrow Doppler-free saturation features (Lamb dips) with the FS-CRDS method centered on the respective transitions, thus providing high resolution measurements of the line centers. The four Lamb-dip spectra are shown in the inset of Fig. 3. Each Lamb dip has a full-width at half-maximum (FWHM) ≈ 0.5 MHz and can be located to better than 0.05 MHz. The Gaussian-fit and Lamb dip methods for line center determination give results differing in magnitude by 0.4 MHz to 1.5 MHz. Given that the Doppler profile is

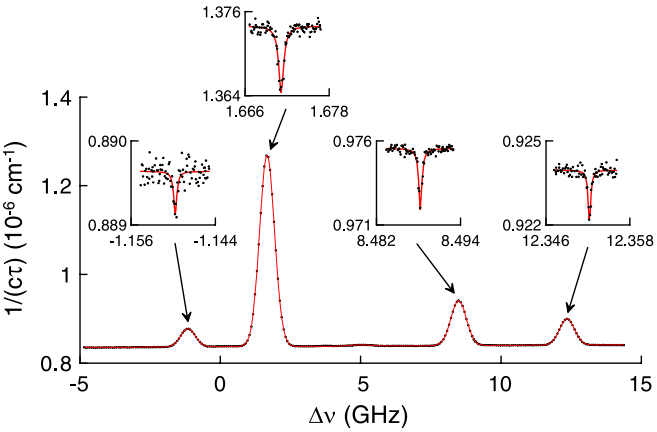

FIGURE 3 Low-pressure spectrum of water vapor (*symbols*) and Gaussian fits (*solid lines*) near $\lambda = 1.392$ μm corresponding to transitions A, B, C and D, occurring from left to right, respectively. Water vapor concentration $n_a = 9.4\times10^{12}$ molecules cm^{-3}, total pressure $p = 38.3$ mPa. The Lamb-dips for each transition are shown in the *inset spectra*. $\Delta\nu = \nu - \nu_0$, $\nu_0 = 214.55430$ THz

≈ 1000 times broader than the Lamb-dip, fit uncertainty in the Gaussian fit contributes significantly to the combined uncertainty in the line center. Specifically, the Gaussian fit method yielded uncertainties in line centers 3 to 8 times greater than those based on the Lamb-dip measurements. Table 3 gives the measured and previously reported relative positions $\nu_A - \nu_B$, $\nu_C - \nu_B$ and $\nu_D - \nu_B$. The Lamb-dip-based FS-CRDS measurements of these relative positions differ in magnitude from HITRAN 2004 values [13] by 9 MHz to 19 MHz. Taking into account the uncertainty in the Lamb dip locations, the frequency detuning axis, and the fit uncertainties, the standard combined uncertainties in the positions of transitions A,

transition	$(\nu_i - \nu_B)_{LD}$ (GHz)	$u(\nu_i - \nu_B)_{LD}$ (MHz)	$(\nu_i - \nu_B)_G$ (GHz)	$u(\nu_i - \nu_B)_G$ (MHz)	$(\nu_i - \nu_B)_{HT}$ (GHz)	$\Delta\delta\nu_i$ (MHz)
A	−2.82088	0.14	−2.81936	1.12	−2.8120	−8.86
B	0		0		0	0
C	6.81718	0.24	6.81619	0.65	6.8031	14.03
D	10.68104	0.36	10.68061	1.06	10.6624	18.64

TABLE 3 Zero-pressure transition frequency differences determined from FS-CRDS measurements of: (1) Lamb dips (LD) and (2) Gaussian profile (G) fits. $\Delta\delta\nu_i$ corresponds to the difference in relative positions between the present measurements $(\nu_i - \nu_B)_{LD}$ and the $(\nu_i - \nu_B)_{HT}$ values reported in [13]. The uncertainties include the fit uncertainty and $u_c(\Delta\nu)$ given in Table 2

C and D relative to transition B are 140 kHz, 240 kHz and 360 kHz, respectively. The differences between our relative positions and these previously reported values significantly exceed our uncertainties, and are likely driven by uncertainty in the HITRAN 2004 data. We recognize that the occurrence of Lamb-dips at this low pressure condition means that profiles outside of the Lamb-dip region likely exhibited some distortion arising from saturation effects. In this article, we ignored these effects, choosing to focus on the Lamb dips as a highly precise marker for line centers. The detailed treatment of saturation effects in ring-down signals is outside the scope of this article, and we refer the reader to previous discussions [28, 29]. Finally, we looked for saturation effects in the ring-down signals and in Doppler-limited spectra at the condition $p = 133$ Pa (1 Torr). These investigations involved varying the incident beam power over a three-fold intensity range. The ring-down signals and the spectra acquired at these conditions showed no evidence of saturation. Thus we conclude that the saturation effects played no role in the much higher-pressure spectra discussed below.

4.2 *Line shape models*

The upper panel in Fig. 4 shows a set of four FS-CRDS spectra for the pressure conditions: $p_1 = 6.67$ kPa, $p_2 = 13.3$ kPa, $p_3 = 26.6$ kPa and $p_4 = 53.3$ kPa. The maximum signal-to-noise ratio (SNR) (defined with respect to the peak absorption loss) for these spectra is $\approx 2100:1$. Line blending becomes pronounced with increased pressure, to the point at which transition A can not be readily seen by simple inspection. To compare the influence of line shape models on the measurements, four different models were fit to the data. These include: 1) Voigt profile (VP) based on fixed Doppler width, 2) Voigt profile (with variable Gaussian width) (VPVG), 3) Galatry profile (GP), and finally 4) speed-dependent Nelkin–Ghatak profile (SDNGP). The corresponding residuals for the $p = 13.3$ kPa case are shown in the bottom panel of Fig. 4. Although there are many other line shape models in the literature, the present treatment is not intended to be exhaustive. Instead we focused on a small number of relatively simple models to illustrate how their differences in line shape can alter the determination of line intensities.

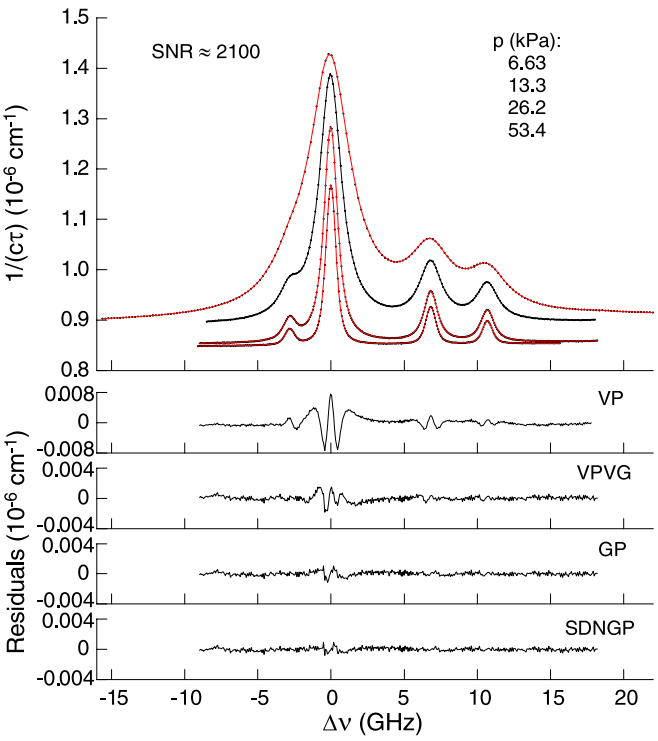

FIGURE 4 Water vapor spectra near $\lambda = 1.392\,\mu$m corresponding to pressure broadening by N_2, with $x_w \approx 6.6 \times 10^{-6}$ $\Delta\nu = \nu - \nu_0$, $\nu_0 = 214.55591$ THz. (**a**) Measured spectra (*symbols*) and SDNGP fits (*solid lines*) for each indicated pressure. (**b**) Fit residuals at $p = 13.33$ kPa condition for indicated spectral line shape models

Details regarding the physical significance of these models have been previously discussed [5], and a more complete review of semiclassical line shape models can be found in [30]. Briefly, the VP represents the convolution of Doppler and Lorentzian profiles and does not account for collisional narrowing or dependence of collisional broadening and shifting on absorber speed (the speed-dependent effects) [31]. The GP [32] is based on the soft-collision model and generalizes the VP to account for Dicke narrowing effects. The VPVG corresponds to a VP in which the Doppler width is allowed to vary in the curve fits. This approach relaxes the physical constraint on the Doppler width and provides an extra degree of freedom in the line shape. However, the VPVG does not have a sound physical basis. The speed-dependent Nelkin–Ghatak profile (SDNGP) [33, 34], incorporates the effects of collisional narrowing in the hard-collisions model and speed-dependent broadening and shifting, and can in general lead to asymmetric line shapes. We note that evaluation of the SDNGP requires that pressure-shifting of the line be measured or estimated. Note that all four line shape models considered here have the collisional full-width at half-maximum Γ as a parameter. Further, the GP and SDNGP models, which account for the effects of collisional narrowing, require a narrowing parameter ν_{opt} known as the optical frequency of velocity-changing collisions. To model the speed-dependence of collisional broadening and shifting we used quadratic functions, see [35], with independent speed-dependent parameters for broadening and shifting that were determined from a multi-spectrum fit of data over the entire range of pressures investigated.

The residual plots in Fig. 4 illustrate that the SDNGP gives the best fit to the measurements, and consequently we considered the SDNGP to give the best value for the area and line intensity of each transition. Taking the SDNGP as the reference case, we compared the models in the following way. We define the fractional difference in the fitted area $\Delta A = (A_j - A_{SDNGP})/A_{SDNGP}$ to quantify systematic deviations in the line area when different models are fit to the same data. As shown in Fig. 5 for transition B, ΔA depends strongly on pressure for the GP and VPVG profiles, with results that can either underestimate or overestimate the SDNGP-based line area (depending on the pressure condition) by up to 1%. A for the VP line shape systematically overestimates the area by more than 2%. Importantly the VP, VPVG and GP models contribute systematic uncertainties greater than the combined uncertainty (shown below) of the FS-CRDS measurement of peak area.

4.3 *Pressure broadening and shifting*

All spectra in Fig. 4 were referenced to a common absolute frequency axis in order to determine absolute pressure shifting of the transitions. To this end the probe laser frequency at the beginning of each scan was measured with the wavelength meter described above. This approach gave an absolute shift coefficient $\delta = (\nu(p) - \nu(p=0))/p$ for transition B of $-1.56(28)\,\mathrm{MHz\,kPa^{-1}}$, with an uncertainty limited by the precision of the wavelength meter. Although δ_B had a relatively high uncertainty, the differential pressure shift coefficients $\delta_i - \delta_B$ were independent of the wavelength meter measurements and exhibited lower uncertainties set by the accuracy of the FS-CRDS detuning axis discussed above.

The line shape parameters Γ and ν_{opt} should scale linearly with pressure for each transition, corresponding to the respective pressure-independent coefficients $\gamma = \Gamma/(2p)$ and $\eta_{\mathrm{opt}} = \nu_{\mathrm{opt}}/p$. However, with regard to Γ not all line shape models considered here yielded results exhibiting this expected behavior. We found that over the pressure range of the measurements the SDNGP gave the most linear dependence of Γ on pressure and the VPVG gave the most nonlinear dependence of Γ. For the SDNGP line shape, we compared γ values as determined by a multi-spectrum fit to the spectra shown in Fig. 4 (with fixed coefficients γ and η_{opt} over the pressure range) against the γ resulting from fits of the individual spectra. Both analyses gave values for γ agreeing within 1%, thus illustrating the weak pressure dependence of the broadening coefficient determined using the SDNGP model. In contrast for the VPVG, as shown in Fig. 6, the fit-derived values of γ depended strongly on the pressure range considered. Specifically, γ changed by 11.8%, 8% and 3.7% based on respective spectral fits for the sets of pressures (p_1), (p_1, p_2), and (p_1, p_2, p_3), compared to the values based on fits using spectra acquired at all 4 pressures (p_1, p_2, p_3, p_4). For the GP, γ differed only slightly from the SDNGP-derived value (see Fig. 4) and showed a dependence on pressure that was ≈ 6 times smaller than for the VPGV.

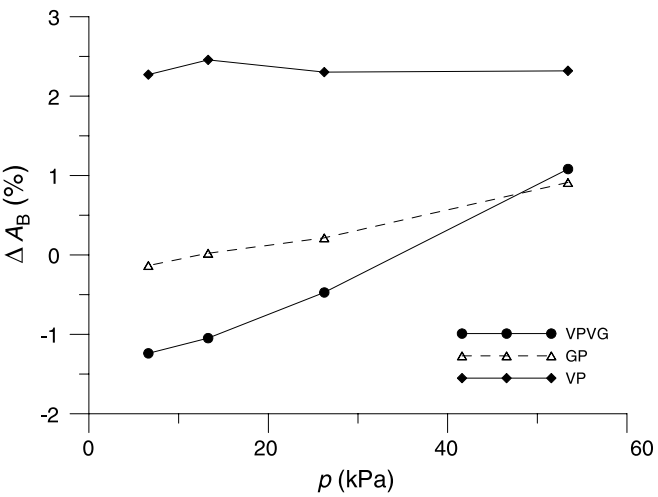

FIGURE 5 Pressure dependence of the fractional difference in the fitted area ΔA_b. Differences are calculated relative to the peak area based on the SDNGP line shape model

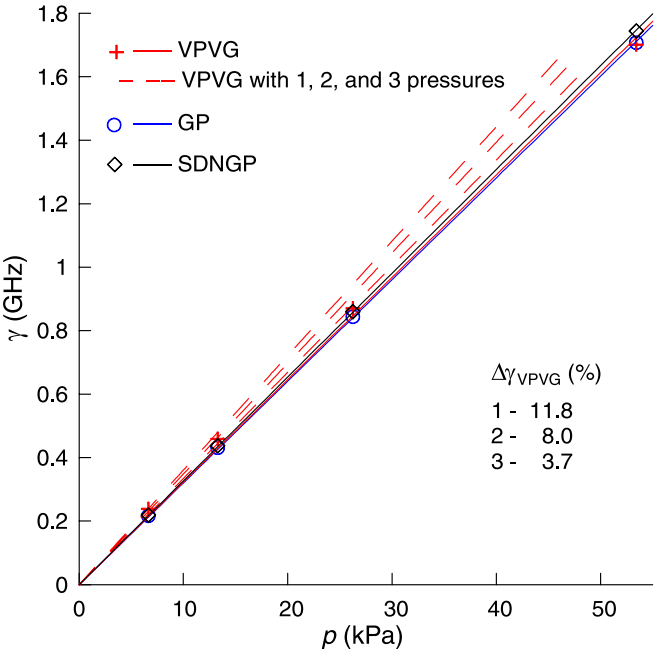

FIGURE 6 Fitted Lorentzian width Γ for the various line shape models considered

transition	HITRAN 2004 γ	γ_{air}	$\gamma/\gamma_{\mathrm{air}}$	Δ_i
A	28.35(15)	24.56	1.154	1.48(7)
B	32.85(7)	29.32	1.120	0
C	33.54(10)	29.00	1.157	0.82(3)
D	31.14(11)	26.27	1.185	1.47(4)

TABLE 4 Measured pressure-broadening coefficients γ defined in terms of half-width at half-maximum of Lorentzian width, and differential pressure shifting coefficients defined as $\Delta_i = \delta_i - \delta_B$. γ and Δ_i values are based upon fits of the SDNGP line shape model to the measured spectra. The absolute shift of transition B is given by $\delta_B = -1.56(28)$ MHz/kPa. HITRAN 2004 values for γ correspond to pressure broadening by air. All quantities (except $\gamma/\gamma_{\mathrm{air}}$ which is dimensionless) are expressed in $(\mathrm{MHz\,kPa^{-1}})$. To convert to commonly used units multiply these quantities by 3.37984×10^{-3} $(\mathrm{cm^{-1}atm^{-1}})/(\mathrm{MHz\,kPa^{-1}})$

Pressure-broadening and differential shift coefficients resulting from the SDNGP fits are given in Table 4. For comparison, we also show the air-broadened values given in HITRAN 2004.

4.4 *Line intensities*

The line intensity S_B was measured at the $p = 13.3$ kPa condition. To this end, the line area A_B was determined by fitting the SDNGP to the FS-CRDS spectra (not shown) limited to the vicinity of transition B. Four spectra were obtained, and the results are summarized in Table 5. For transition B, which was by far the strongest transition, the largest uncertainty component arose from the generation and measurement of n_a. This was limited by the accuracy of the CMH used to measure the water vapor molar fraction in the sample gas. The net water vapor background molar fraction $x_{\mathrm{w,bg}}$, which must be added to the CMH measurement of x_{w}, was found by bypassing the water vapor source of the PTMG and measuring the absorption spectrum of residual wa-

transition	$\tilde{\nu}$ (cm^{-1})	S_i (10^{-21} cm molecule^{-1})	$u_{c,r}(S_i)$ (%)	$S_{i,\mathrm{HT}}$ (10^{-21} cm molecule^{-1})	$u_{\mathrm{c,r}}(S_{\mathrm{HT}})$ (%)	$(S_{i,\mathrm{HT}} - S_i)/S_i$ (%)	$u_{\mathrm{c,r}}(A_i)$ (%)	$a_{i,B}$	$\sigma(a_{i,B})/a_{i,B}$ (%)
A	7156.723	0.0983	0.89	0.0996	2	1.3	0.71	0.0910	0.65
B	7156.817	1.0804	0.61	1.0730	1	−0.68	0.28	1	
C	7157.044	0.2547	0.66	0.2554	1	0.28	0.39	0.2357	0.26
D	7157.173	0.1500	0.69	0.1513	2	0.85	0.44	0.1389	0.33

TABLE 5 Line intensity results referenced to $T = 296$ K. $S_{i,\mathrm{HT}}$ are HITRAN 2004 values reported in [13]. The reported uncertainties for S_i combine $u_{c,r}(A_i)$ and $u_{c,r}(n_{\mathrm{w}})$, where the former is the combined relative uncertainty in the measurement of A_i which includes $u_r(g) = 0.2\%$, $u_r(\delta\nu)$, and the standard deviation of repeated measurements. $a_{i,B} = A_i/A_b$ represents the mean area ratio for the respective transitions, and $\sigma(a_i)$ is the standard deviation of the measured area ratios for the set of 4 pressure conditions

ter vapor in the ring-down cell. This background spectrum was taken at the same pressure and flow rate condition as for the line intensity measurement. To improve sensitivity the water vapor transition at $\tilde{\nu} = 7170.2778\,\mathrm{cm}^{-1}$ was probed, giving $x_{\mathrm{w,bg}} \approx 30\,\mathrm{nmol\,mol}^{-1}$, while typical values of x_{w} during the line intensity measurements were $6.7\,\mu\mathrm{mol\,mol}^{-1}$. The combined relative uncertainty in S_B was 0.61%, whereas the relative uncertainty contribution in the measurement of A_B was only 0.28%, thus indicating that the present measurements of S_B were not limited by the FS-CRDS technique. This result also illustrates the potential of FS-CRDS for making high-accuracy line intensity determinations for inert sample gases (CO_2, O_2, low-molecular weight hydrocarbons etc.) for which it should be possible to minimize uncertainties in sample concentration. We also note that unlike the situation for measuring frequency differences where there is an appreciable cumulative error associated with $u(\Delta\nu)$, the uncertainty in frequency detuning has a negligible effect on determination of the line areas. In the present work, this quantity contributed to line intensity uncertainty on a relative basis as $u(\Delta\nu)/\mathrm{FSR} = 0.025\%$.

The remaining line intensities were based on the measured value of S_B and the area ratios, $a_{i,B} = \mathrm{A}_i/\mathrm{A}_b$ ($i = A, C, D$) for the set of 4 spectra given in Fig. 4. Here $S_i = S_B a_{i,B}$. Note that $a_{i,B}$ is insensitive to systematic uncertainty in n_{a}, and therefore provides a measure of the linearity and consistency of the spectroscopic measurements of line area with respect to changes in gas pressure. We found that $a_{i,B}$ had a relative standard deviation $\sigma(a_i)/a_i$ ranging from 0.65% to 0.26%. The spectra of the other transitions exhibited degraded precision. This trend, which was indicated by increasing $u_{c,r}(\mathrm{A}_i)$ with decreasing line intensity, is consistent with signal-to-noise considerations in the spectra. All things being equal the relative uncertainty in the determination of a line area scales as $(\sigma_{k,b}/k_b)(1 + k_b/k_a)N^{-1/2}$, where $\sigma_{k,b}/k_b$ is the relative standard deviation in the base-loss cavity decay rate, and N is the number of points in the fitted spectrum [36]. Consequently, as the line intensity decreases, k_b/k_a increases and the SNR of the line decreases, thus increasing type A uncertainties in the ring-down spectrum. Conversely, $u_r(S_i)$, ($i = A, C, D$) could be reduced to that of transition B by measurement at elevated values of x_{w} that give peak losses comparable to those of transition B in the present case. Finally we note the good agreement between our measured line intensities and the values reported in the HITRAN 2004 database. The relative differences in line intensity range in magnitude from 0.28% to 1.3%, and are consistent with the combined uncertainties of both sets of measurements.

5 Conclusion

Using the FS-CRDS technique, we have measured differential pressure shifting coefficients, pressure broadening coefficients and line intensities for blended rovibrational transitions of water vapor. As a consequence of its high-spectral resolution ($\delta\nu < 50$ kHz), we have demonstrated that the FS-CRDS method can be used to measure subtle changes in line shape and line position of composite spectra. The line intensity results compare favorably with the most accurate values obtained using high-resolution ($\delta\nu < 300$ MHz) long-path Fourier-Transform spectrometer (FTS) systems. In this investigation, the accuracy of the measured line intensity was limited primarily by our ability to prepare a known quantity of water vapor in the sample gas. However, the present results suggest that FS-CRDS methods will yield line intensities with relative uncertainties at the 0.25% or better for other species where sample preparation is not a limiting factor. Further, we exploited the high-spectral resolution of FS-CRDS by probing Doppler-free Lamb dips to locate relative line positions in closely space transitions. Although not shown explicitly here, this approach will work even for spectra whose Doppler-limited lines overlap provided the line centers are separated by more than the width of the Lamb dip (≈ 1 MHz). The measurement of line centers by Lamb-dip spectroscopy provides a strong constraint when fitting blended spectra where line positions would otherwise be highly uncertain.

For non-blended transitions, the saturation dips presented here also illustrate that FS-CRDS can be used to locate component transition frequencies with a precision approaching the linewidth of the ring-down cavity. However, in this experiment the accuracy of the absolute line positions and pressure shifting coefficients was limited by the relatively large uncertainty in the wavelength meter which was used for determining the absolute frequency of the probe laser. With regard to pressure shifts, we have recently demonstrated an improved approach using the FS-CRDS technique [27] that is not limited by imprecision in the wavelength meter. Further, the current limiting factor in the determination of absolute transition frequencies is not fundamental and can be mitigated by using an optical frequency-comb as a frequency reference [37]. This approach would enable improved determination of the cavity FSR and probe laser frequency, yielding absolute transition frequencies with uncertainties approaching the kHz-level linewidth of the frequency-stabilized ring-down cavity.

ACKNOWLEDGEMENTS The authors would like to thank Gregory E. Scace for calibration of the chilled-mirror hygrometer and

Dr. Keith A. Gillis for assistance in measuring the acoustical noise in the ring-down cell. This work was supported by the NIST Office of Microelectronics Programs.

REFERENCES

1 G. Di Stefano, Chem. Phys. **302**, 243 (2004)
2 V. Malathy Devi, D.C. Benner, M.A.H. Smith, L.R. Brown, M. Dulick, J. Quant. Spectrosc. Radiat. Transf. **76**, 393 (2003)
3 C.E. Miller, L.R. Brown, R.A. Toth, D.C. Benner, V. Malathy Devi, Comp. Rendus Phys. **6**, 876 (2005)
4 C. Chackerian, R. Freedman, L.P. Giver, L.R. Brown, J. Mol. Spectrosc. **210**, 119 (2001)
5 D. Lisak, J.T. Hodges, R. Ciuryło, Phys. Rev. A **73**, 012 507 (2006)
6 J.T. Hodges, D. Lisak, Appl. Phys. B **85**, 375 (2006)
7 X. Zhou, J.B. Jeffries, R.K. Hanson, Appl. Phys. B **81**, 711 (2005)
8 E.R.T. Kerstel, R.Q. Iannone, M. Chenevier, S. Kassi, H.-J. Jost, D. Romanini, Appl. Phys. B **85**, 397 (2006)
9 M. Lepère, A. Henry, A. Valentin, C. Camy-Peyret, J. Mol. Spectrosc. **208**, 25 (2001)
10 L. Moretti, A. Sasso, L. Gianfrani, R. Ciuryło, J. Mol. Spectrosc. **205**, 20 (2001)
11 R.A. Toth, J. Quant. Spectrosc. Radiat. Transf. **94**, 1 (2005)
12 R.A. Toth, J. Quant. Spectrosc. Radiat. Transf. **94**, 51 (2005)
13 L.S. Rothman, D. Jacquemart, A. Barbe, D.C. Benner, M. Birk, L.R. Brown, M.R. Carleer, C. Chackerian Jr., K. Chance, L.H. Coudert, V. Dana, V. Malathy Devi, J.-M. Flaud, R.R. Gamache, A. Goldman, J.-M. Hartmann, K.W. Jucks, A.G. Maki, J.-Y. Mandin, S.T. Massie, J. Orphal, A. Perrin, C.P. Rinsland, M.A.H. Smith, J. Tennyson, R.N. Tolchenov, J. Vander Auwera, P. Varanasi, G. Wagner, J. Quant. Spectrosc. Radiat. Transf. **96**, 139 (2005)
14 J.T. Hodges, H.P. Layer, W.W. Miller, G.E. Scace, Rev. Sci. Instrum. **75**, 849 (2004)
15 J.T. Hodges, R. Ciuryło, Rev. Sci. Instrum. **76**, 023 112 (2005)
16 J. Morville, S. Kassi, M. Chenevier, D. Romanini, Appl. Phys. B **80**, 1027 (2005)
17 V. Motto-Ros, J. Morville, P. Rairoux, Appl. Phys. B, ISSN 1432-0649 (2007, Online)
18 G.E. Scace, J.T. Hodges, *Uncertainty of the NIST Low Frost-Point Humidity Generator*, In: *Proc. International Symposium on Temperature and Thermal Measurements in Industry and Science* (TEMPMEKO 2001) (VDE Verlag, Berlin, 2002), pp. 597–602
19 R.W. Hyland, A. Wexler, J. Res. NBS **77**, 115 (1973)
20 A. Wexler, J. Res. NBS **81**, 5 (1977)
21 T. Gherman, D. Romanini, Opt. Express **10**, 1033 (2002)
22 T. Gherman, D. Romanin, I. Sagnes, A. Garnache, Z. Zhang, Chem. Phys. Lett. **383**, 353 (2004)
23 M.J. Thorpe, R.J. Jones, K.D. Moll, J. Ye, Opt. Express **13**, 882 (2005)
24 M.J. Thorpe, K.D. Moll, R.J. Jones, J. Ye, Science **311**, 1595 (2006)
25 K.K. Lehmann, *Dispersion and Cavity-Ringdown spectroscopy*, In: *Cavity-Ringdown Spectroscopy: An Ultratrace-Absorption Measurement Technique*, ed. by K.A. Busch, M.A. Busch (University Press, Oxford, UK, 1998), Chapt. 8
26 P.E. Ciddor, Appl. Opt. **35**, 1566 (1996)
27 D.J. Robichaud, J.T. Hodges, D. Lisak, C.E. Miller, M. Okumura, J. Quant. Spectrosc. Radiat. Transf., in press (2007)
28 S.S. Brown, H. Stark, A.R. Ravishankara, Appl. Phys. B **75**, 173 (2002)
29 J.Y. Lee, J.W. Hahn, Appl. Phys. B **79**, 653 (2004)
30 R. Ciuryło, Phys. Rev. A **58**, 1029 (1998)
31 P.R. Berman, J. Quant. Spectrosc. Radiat. Transf. **12**, 1331 (1972)
32 L. Galatry, Phys. Rev. **122**, 1218 (1961)
33 S.G. Rautian, I.I. Sobelman, Usp. Fiz. Nauk **90**, 209 (1966) [Sov. Phys. Uspekhi. **9**, 701 (1967)]
34 B. Lance, G. Blanquet, J. Walrand, J.-P. Bouanich, J. Mol. Spectrosc. **185**, 262 (1997)
35 D. Priem, F. Rohart, J.M. Colmont, G. Wlodarczyk, J.P. Bouanich, J. Mol. Struct. **517**, 435 (2000)
36 R.D. van Zee, J.T. Hodges, J.P. Looney, Appl. Opt. **38**, 3951 (1999)
37 J. Ye, S.T. Cundiff, In: *Femtosecond Optical Frequency Comb Technology*, ed. by J. Ye, S.T. Cundiff (Springer, New York, 2005), p. 12